Influence mechanism of Pd, Pt, Rh/γ-Al$_2$O$_3$ on NH$_3$ formation for NO reduction by CO

Houlin Wang, Yue Peng [*], Wenzhe Si, Chuan Gao, Yunlong Wang, Rong Wang, Jin Yuan, Bin Zhou, Junhua Li [*]

State Key Joint Laboratory of Environment Simulation and Pollution Control, School of Environment, Tsinghua University, Beijing 100084, China

ABSTRACT

The byproducts of NO reduction by CO have attracted great interest in the three-way catalysts, but the influence of active components (Pd, Pt, and Rh) on the formation mechanism is still elusive. Herein, Pd/, Pt/, and Rh/Al$_2$O$_3$ were prepared for investigating the NH$_3$ formation during NO reduction by CO under wet conditions. The strongest metal-support interaction in Rh/Al$_2$O$_3$ is attributed to the highest interfacial Rh–O–Al bond from the results of XAFS and NMR. The smallest particle size and highest redox property on Rh/Al$_2$O$_3$ led to the highest NH$_3$ yield below 300 °C. Pt/Al$_2$O$_3$ produced more NH$_3$ than Pd/Al$_2$O$_3$ above 350 °C because of robust response to lattice oxygen reacted with NO and reduction by CO. The optimal strategy for minimizing byproducts on the premise of preserving three-way catalyst performance was the PtRh/γ-Al$_2$O$_3$ where the molar ratio of Pt: Rh was 9:1.

1. Introduction

The three-way catalyst (TWC) is extensively employed to control CO, hydrocarbons (HCs), and NO$_x$ emissions in gasoline vehicles. Platinum (Pt), palladium (Pd), and rhodium (Rh) supported on γ-Al$_2$O$_3$ facilitate the oxidation of CO and HCs to CO$_2$ during the fuel-lean working conditions and the reduction of NO$_x$ to N$_2$ during the fuel-rich working conditions, meeting increasingly stringent emission standards.[1] Recently, it is reported that some byproducts (for example N$_2$O and NH$_3$) also form on the TWC primarily in fuel-rich working conditions.[2,3] An investigation revealed that the NH$_3$ production of on-road gasoline vehicles varied from 2 to 48 mg/km.[4–6] It is foreseen that the China 7 or Euro 7 standards will be more stringent on N$_2$O and NH$_3$ emissions.[7,8] It is crucial to note that their formation, especially NH$_3$, is closely related to the air-fuel ratio (λ) and TWC active components, which is controlled by the water-gas shift (WGS) and HCs reforming reactions in reducing atmospheres (λ<1).[9–11] Both reactions generate strong reductants (H$_2$), capable of reducing NO$_x$ to N$_2$ but also leading to undesired byproducts. Consequently, the reduction of NO by CO emerges as a crucial model in TWC.[12–16] Thereby, it is becoming important to elucidate the formation of NH$_3$ in NO reduction and provide a strategy to minimize the emission by optimizing the TWC.

The γ-Al$_2$O$_3$ not only presents a big surface area and thermal resistance to stabilize platinum group elements (PGMs) but also provides both intrinsic Lewis acid sites from different coordinated Al cations and Brönsted acid sites from various kinds of surface hydroxyls. In general, Pt/Al$_2$O$_3$ and Pd/Al$_2$O$_3$ exhibit high activities in oxidizing CO and HCs to CO$_2$, while Rh/Al$_2$O$_3$ is employed to reduce NO$_x$. The particle size of PGMs and coordination environments also play a pivotal role in determining distinct product selectivity. For instance, an Rh nanoparticle usually produced methane, while an Rh single atom yielded CO in CO$_2$ reduction.[17,18] Researchers attributed this size dependency to the preferential formation of hydroxyls on Rh clusters. Furthermore, it has been observed that Pt-based catalysts exhibit minimal primary N$_2$O formation during HCs oxidation, whereas Pd-based catalysts generate N$_2$O up to 500 °C.[2] It has been found that decreasing the loading or increasing the grain size of PGMs is feasible to diminish byproducts, but it comes at the cost of suppressing TWC performance [19,20]. Therefore, the design strategy of TWC to reduce the byproduct formations while maintaining TWC performance is still the ongoing discussion and development.

The metal-support interaction (MSI) of PGMs on γ-Al$_2$O$_3$ plays a critical role in determining cluster morphology and dispersion by adjusting the electron transfer and surface oxygen migration.[21] The deposition of PGMs with preferential orientation on the same support, or the load of the same PGMs onto different crystallized supports, also
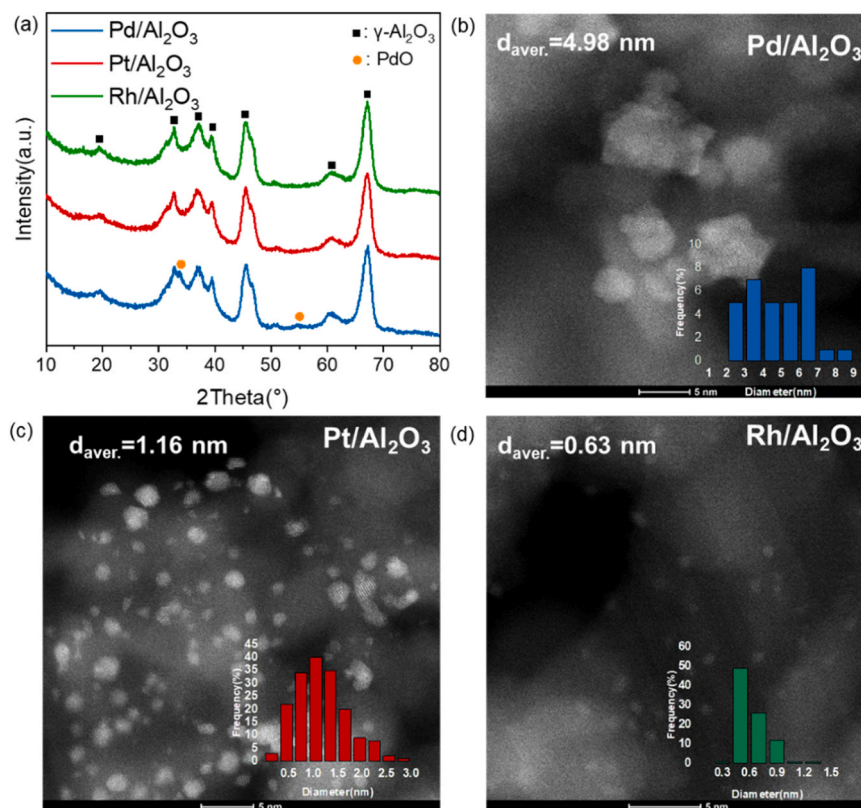
Fig. 1. XRD (a), STEM images and particles sizes of Pd/Al$_2$O$_3$ (b), Pt/Al$_2$O$_3$ (c), and Rh/Al$_2$O$_3$ (d).

impacts the activity of products and the pathways of reactions.[22] In terms of dispersion modification, inert additions such as BaO prefer to bond with 5-coordinated Al of γ-Al$_2$O$_3$ to create additional Al cations, facilitating the redispersion of active sites.[23] Furthermore, PGMs can also exchange protons with both acidic and basic hydroxyls on γ-Al$_2$O$_3$. Proton exchange was promoted by H$_2$O, hastening the formation of well-dispersed PGMs species by creating hydroxyls adjacent to 4 or 6-co-ordinated aluminum.[24–26] However, the MSI of PGMs and γ-Al$_2$O$_3$ as well as influence mechanism on byproduct formations in NO reduction remain unclear.

Here, we investigated the surface anchoring differences of Pt, Pd, and Rh (~1.0 wt%) onto 4, 5, and 6-coordinated Al on γ-Al$_2$O$_3$ and their formation mechanisms of NH$_3$ under simulated TWC flue gas. [1]H and [27]Al nuclear magnetic resonance (NMR) spectra and extended X-ray absorption fine structure (EXAFS) results revealed that the MSI of PGMs and γ-Al$_2$O$_3$ can be due to interfacial PGMs–O–Al bond formation. Furthermore, in-situ diffuse reflectance infrared Fourier transform spectroscopy (In-situ DRIFTS) and X-ray photoelectron spectroscopy (in-situ NAP-XPS) were employed to elucidate intermediate species and electron transfers during byproduct formation. Finally, an optimal strategy for minimizing byproduct formation has been proposed and suggested the components (Pt$_{0.9}$Rh$_{0.1}$ supported on γ-Al$_2$O$_3$) that show superb byproduct suppression under simulated TWC flue gas.

2. Experiments

2.1. Catalyst synthesis

The catalysts were synthesized by a vacuum rotary impregnation method. The Pt(NO$_3$)$_2$ (Heli Precious Metals Technology (China) Co., Ltd), Pd(NO$_3$)$_2$·2 H$_2$O (Aladdin), Rh(NO$_3$)$_3$ (Macklin), and γ-Al$_2$O$_3$ (nano- Al$_2$O$_3$, Macklin, average size 40 nm, 152.4 m^2/g). The 2.0 g γ-Al$_2$O$_3$ was introduced into an aqueous solution of PGMs according to the amount of wt. 1%. After stirring for 2 h at room temperature, the

suspension was transferred to a flask in a water bath at 40 °C for 1 h and then the water was removed through vacuum rotary evaporation. The obtained powder samples were dried at 100 °C overnight and then calcined at 500 °C for 2 h in air. The reference samples, PtRh/Al$_2$O$_3$ and PdRh/Al$_2$O$_3$, were prepared using the same method. The content of noble metals in both catalysts constituted 1% by weight, with molar ratios of Pt:Rh and Pd:Rh set at 9:1.

2.2. Performance test

The N$_2$O and NH$_3$ formation efficiencies during TWC reactions were evaluated by the Gasmet DX4000 gas analyzer, monitoring concentration of the effluent gases (N$_2$O, NO, NO$_2$, CO, CO$_2$, NH$_3$, and H$_2$O). The evaluations of NO+CO, WGS reactions, and temperature-programmed desorption (TPD) of CO and NO were also conducted on the same system. Before each test, 50 mg of catalysts were blended with 100 mg of silica pellets (40–60 mesh) to mitigate the impact of hot spots. The total gas flow rate was set at 200 mL·min^{-1} with the gas hourly space velocity (GHSV) 240,000 mL·g^{-1}·h^{-1}. More details are provided in supplementary information (**SI**).

2.3. Characterizations

The X-ray powder diffraction (XRD) data were obtained on a Rigaku X-ray diffractometer (D/max-2200) fitted with a Cu Kα source (λ = 0.15405 nm, 40 kV, and 200 mA). The Brunauer-Emmett-Teller (BET) surface areas were obtained by N$_2$ adsorption-desorption at the liquid N$_2$ temperature (-196 °C) using a Quantachrome Autosorb-1MP apparatus. Inductively coupled plasma-optical emission spectroscopy (ICP-OES) measurements were performed on IRIS Intrepid II ICP spectrometer (Thermo Scientific, USA). ^{1}H and ^{27}Al NMR spectra were recorded on a JNM-ECZ600R/M1 spectrometer equipped with a 3.2 mm double-resonance probe employing a single pulse method. H$_2$ temperature-programmed reduction (H$_2$-TPR), O$_2$ temperature-programmed
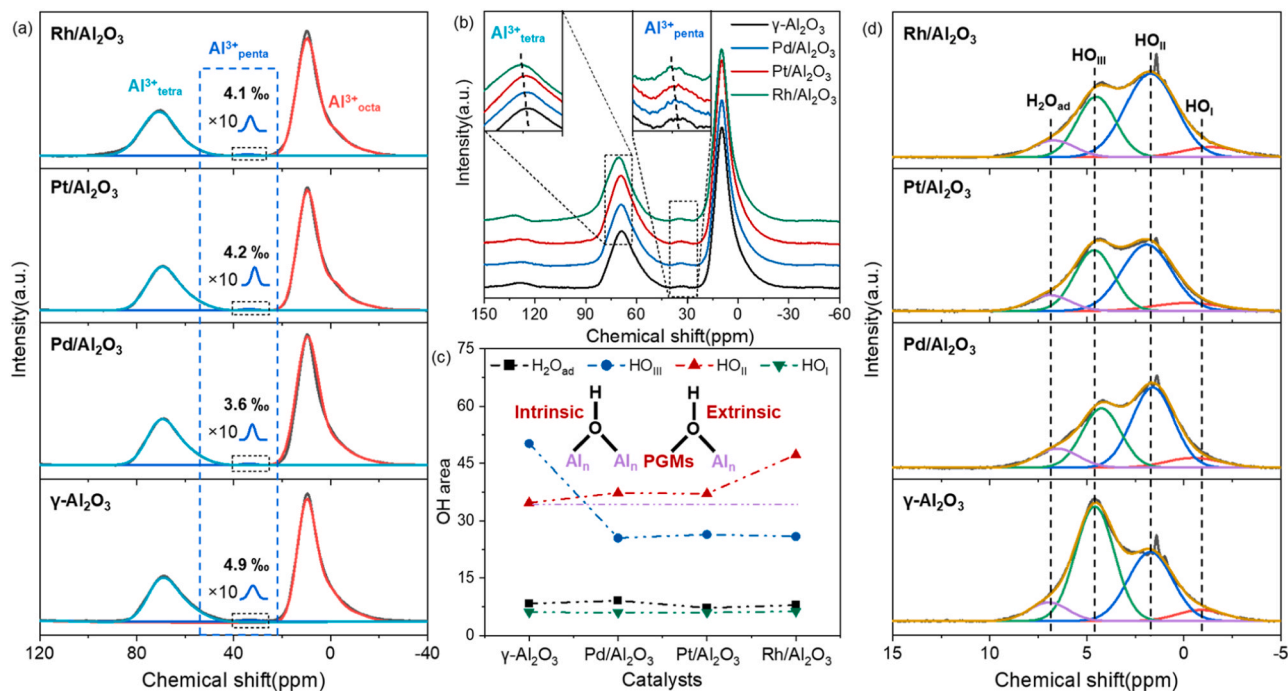
Fig. 2. ^{27}Al NMR spectra: integrating profiles of catalysts(a), original data(b); ^{1}H NMR spectra: integrating area changes of different hydroxyls in γ-Al$_2$O$_3$ and PGMs/Al$_2$O$_3$(c), integrating profiles of catalysts(d). (all samples have been pre-treated in 300 °C for 6 h, γ-Al$_2$O$_3$ has been pre-treated using same process with synthesis of PGMs/Al$_2$O$_3$).

desorption (O$_2$-TPD), and CO-titration measurements were performed on a Micromeritics AutoChem II 2920. XPS measurements for catalysts were performed by using a Thermo Fisher Scientific ESCALAB 250Xi with photoelectron spectroscopy system using Al Kα (1 , 486.6 eV) X-ray source with a spot size of 400 μm^2 and a resolution of 0.05 eV. The binding energy of all peaks was calibrated at 284.8 eV from adventitious carbon (C 1s). Aberration-corrected scanning transmission electron microscopy (STEM) was carried out on an FEI Titan 80–300 electron microscope equipped with a Gatan Enfinium camera system. The X-ray absorption fine spectra (XAFS), including X-ray absorption near-edge structure (XANES) and EXAFS, were collected at the Shanghai Synchrotron Radiation Facility (Shanghai, China), where a pair of channel-cut Si (111) crystals was used in the monochromator. Further details can be found in **SI**.

2.4. In-situ spectroscopies

In-situ DRIFTS was performed on an FTIR (Nicolet IS-50) equipped with an MCT/A detector. All the spectra were recorded in the range 4000–800 cm^{-1} with a resolution of 4 cm^{-1}. Each spectrum was obtained from 16 scans, and background spectra with 32 scans were subtracted from corresponding spectra at different temperatures. Before collection, each sample underwent N$_2$ pre-treatment at 500 °C for 30 minutes. In-situ NAP-XPS were performed on a SPECS NAP-XPS system. Spectra were obtained using monochromatized Al Kα irradiation (1 , 486.6 eV) generated by an Al anode (SPECS XR-50) with an excitation source power fixed at 50 W. The sample heating during the measurement was achieved through contact with a hot sample table heated by electron bombardment from the backside in a vacuum. More details are available in **SI**.

3. Results and discussions

3.1. Catalyst morphology

The X-ray diffraction (XRD) patterns reveal that all catalysts maintain the γ crystalline phase structure of Al$_2$O$_3$ (Fig. 1a). As for the Pd/Al$_2$O$_3$, the weak peaks at 33.8 and 54.7° can be assigned to PdO, suggesting that Pd species present oxidation states with certain crystallization on γ-Al$_2$O$_3$. The STEM and CO-titration (Fig. 1b-d.) unveil the catalysts and the nanoparticle sizes distribution diagram of PGMs. According to the probability distribution, the order of average nanoparticle sizes was as follows: Pd (4.98 nm) > Pt (1.16 nm) > Rh (0.63 nm), the tendency of nanoparticle size coincided with the results of H$_2$-titration experiments (Table S3).

3.2. Influence of PGMs on γ-Al$_2$O$_3$

As known, the loading PGMs on support will change the location environment via MSI and were first studied by ^{1}H and ^{27}Al NMR spectra (Fig. 2a-d). The resonance peaks at 69.1–70.7, 9.8, and 33.6–34.9 ppm can be assigned to the Al^{3+} at 4 and 6-coordinated Al (Al$^{3+}_{tetra}$ and Al$^{3+}_{octa}$) as well as the unsaturated 5-coordinated Al (Al$^{3+}_{penta}$) **in** Fig. 2a & b.[21, 27] Moreover, the ^{1}H NMR spectra can be deconvoluted into 4 peaks, the resonance peaks at −1.0–1.0, 1.0–2.5, 2.5–4.5, and 5.0–8.0 ppm can be assigned to terminal (HO$_I$), doubly bridging (HO$_{II}$), triply bridging (HO$_{III}$) hydroxyls (i.e., basic/acidic hydroxyls, Al^{3+}−OH), and residual water (H$_2$O$_{ad}$) **in** Fig. 2c & d, respectively. [24,28,29] The order of resonances intensity attributed to Al$^{3+}_{penta}$ was as follows: γ-Al$_2$O$_3$ (4.9‰) > Pt/Al$_2$O$_3$ (4.1‰) ≈ Rh/Al$_2$O$_3$ (4.2‰) > Pd/Al$_2$O$_3$ (3.6‰), suggesting that more Pd species are anchored to Al$^{3+}_{penta}$ sites than Pt and Rh. Furthermore, it was also observed that the resonance peaks of Al$^{3+}_{tetra}$ and Al$^{3+}_{penta}$ upshifted after PGMs impregnation **in** Fig. 2 b, the extent of shift is as follows: Rh/Al$_2$O$_3$ > Pt/Al$_2$O$_3$ ≈ Pd/Al$_2$O$_3$ > γ-Al$_2$O$_3$, suggesting that the coordination environment of the surface Al$^{3+}_{tetra}$ and Al$^{3+}_{penta}$ have been influenced by supported PGMs. For Al^{3+}−OH, the area of HO$_{III}$ decreased from 50.2 to about 26 for PGMs/Al$_2$O$_3$ **in** Fig. 2c and Tab. S4, suggesting that the same quantity of Pd, Pt, and Rh atoms are anchored via proton exchange. However, the area of HO$_{II}$ in PGMs/Al$_2$O$_3$ is more than that of γ-Al$_2$O$_3$ **in** Fig. 2c and Tab. S4, which is as follows: Rh/Al$_2$O$_3$ > Pd/Al$_2$O$_3$ > Pt/Al$_2$O$_3$ > γ-Al$_2$O$_3$, indicating that the new hydroxyls (HO'$_{II}$) have formed on the process of PGMs anchoring. According to the

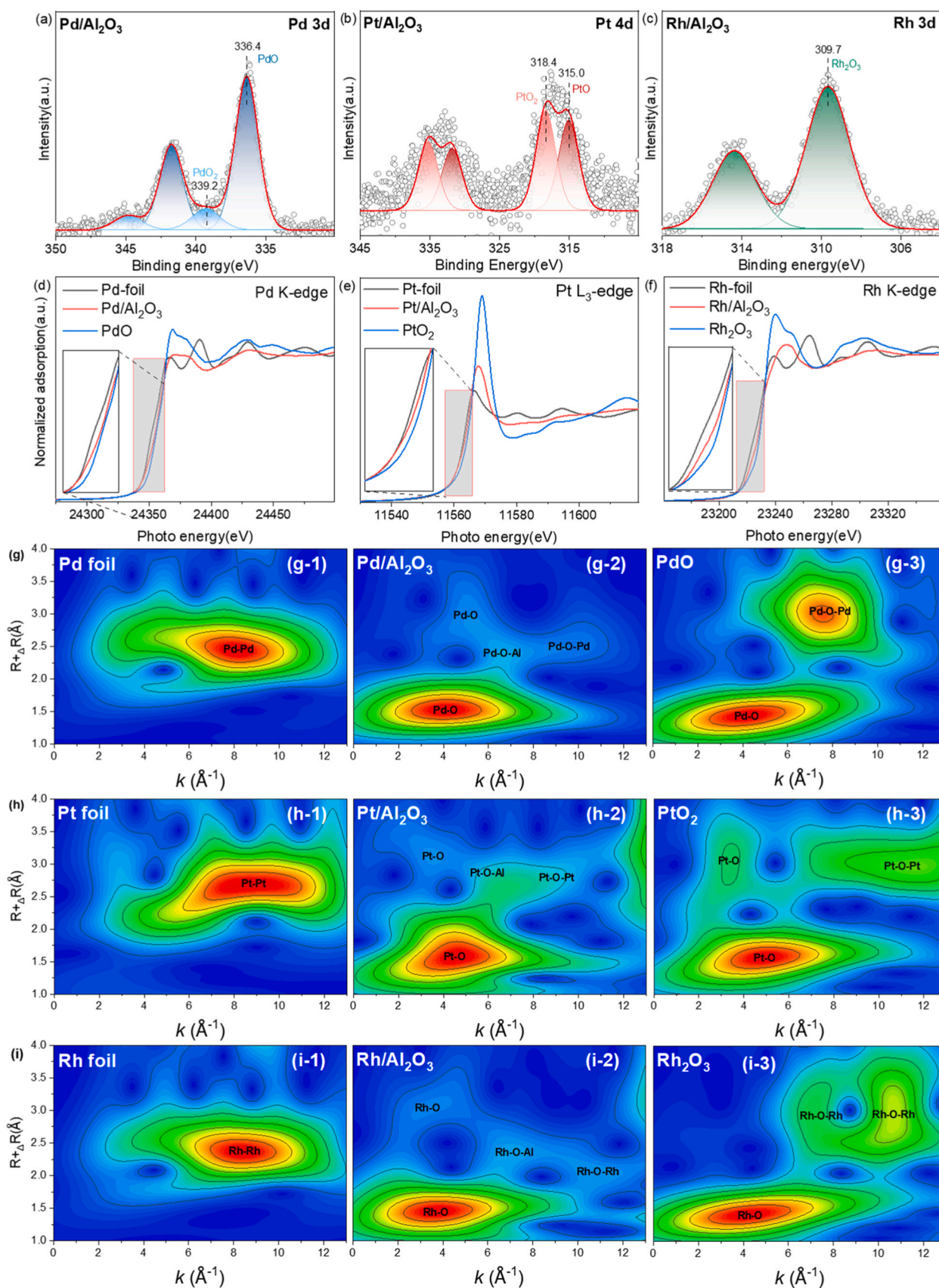**Fig. 3.** Pd 3d (a), Pt 4d (b), and Rh 3d (c) XPS spectra of Pd/Al$_2$O$_3$, Pt/Al$_2$O$_3$, and Rh/Al$_2$O$_3$, respectively. XANES spectra of Pd K-edge(d), Pt L$_3$-edge (e), and Rh K-edge (f); the wavelet transforms (g, h, and i) from experimental data for the catalysts and their corresponding metal foils and oxides.

Table 1
Locations of all lobes from samples and their oxides.

Catalysts	Coordinate points/(X Å^{-1}, Y Å)[a]			
	PGMs−O1	PGMs−O2	PGMs−O−Al	PGMs−O−PGMs
PdO	(4.1, 1.4)			(7.6, 3.0)
Pd/Al$_2$O$_3$	(4.1, 1.5)	(5.2, 3.0)	(6.7, 2.4)	(9.5, 2.5)
PtO$_2$	(5.0, 1.6)	(3.4, 3.1)		(11.0, 3.0)
Pt/Al$_2$O$_3$	(4.7, 1.6)	(3.5, 3.1)	(6.0, 2.9)	(9.1, 2.8)
Rh$_2$O$_3$	(4.2, 1.4)			(7.3, 3.0)
				(10.7, 3.0)
Rh/Al$_2$O$_3$	(3.8, 1.6)	(3.6, 3.0)	(7.2, 2.3)	(11.0, 2.0)

[a] X and Y are from the value of k at the k-space and R at the R-space, respectively.

previous work, the HO'$_{II}$ can be assigned to PGMs−(HO)−Al$_n$.[26] Namely, all PGMs can be anchored by Al$^{3+}_{penta}$ (especially Pd) and Al^{3+}−OH (mainly HO$_{III}$), forming new HO'$_{II}$ in interfacial bond (PGMs−(HO)−Al$_n$) and further slightly changing the coordination environment of Al$^{3+}_{tetra}$ and Al$^{3+}_{penta}$. These changes in surface microstructure could lead to different interactions between PGMs and γ-Al$_2$O$_3$ and will be further discussed below.

3.3. Chemical valence states

The chemical states of PGMs were monitored by XPS and XAFS spectra. The XPS spectra, calibrated at 284.8 eV from C 1s, were fitted and deconvoluted as shown in Fig. 3a-c and Fig. S1a-**f**. The XPS peaks of Pd 3d$_{5/2}$ at 336.4 and 339.2 eV are assigned to PdO and PdO$_2$, the XPS peaks of Pt 4d$_{5/2}$ at 315.0 and 318.4 eV are assigned to PtO and PtO$_2$, and the XPS peak of Rh 3d$_{5/2}$ is assigned to Rh$_2$O$_3$, respectively.[30,31] No metallic species were observed on the XPS spectra, indicating that Pt, Pd, and Rh species on γ-Al$_2$O$_3$ exist in oxidized states. Based on the fitting results, the proportions of Pd^{2+} and Pt^{2+} were approximately 83.3% and 47.4% respectively. Besides the XPS spectra, XANES of Pd K-edge, Pt L$_3$-edge, and Rh K-edge were used to confirm the valence states of PGMs (Fig. 3d-f). The pre-edge of Pd in Pd/Al$_2$O$_3$ was within that of PdO and Pd foil, indicating that the average valence states of Pd in Pd/Al$_2$O$_3$ are within 0–2. Similarly, both Pt in Pt/Al$_2$O$_3$ and Rh in Rh/Al$_2$O$_3$ were in the oxide states. However, the initial section of Pd K-edge (24281–24345 eV) in Pd/Al$_2$O$_3$ and Pt L$_3$-edge (11531–11561 eV) in Pt/Al$_2$O$_3$ almost overlapped the corresponding Pd and Pt foils, respectively. This implies that Pd and Pt species could be metallic state in the inner of nanoparticles, which could result from their bigger nanoparticle sizes compared to Rh. Moreover, this conclusion is also proved by their images of STEM (Fig. S2).

The wavelet transforms of EXAFS on all catalysts are shown in Fig. 3g-i. According to previous studies, the y-axis was denoted as the distance between the centered PGMs and adjacent atoms, while the x-axis was denoted as the existence of that influenced by the adjacent atoms, which was related to atomic numbers (Z). Its position shifted to larger k values with increasing Z values of adjacent atoms, which can be used to distinguish different interaction when the distance presented in R-space was similar.[32–34] The coordination and bond distance of PGMs to oxygen are identified and listed in Table 1. The bond of Pt−O1 at the first shell (red region) in Pt/Al$_2$O$_3$ was close to the position in PtO$_2$, suggesting that Pt species in Pt/Al$_2$O$_3$ are oxide state. Likewise, both Pd species in Pd/Al$_2$O$_3$ and Rh species in Rh/Al$_2$O$_3$ were also oxide states. For oxygen atoms at the second sphere, the k value of Pd−O2 in Pd/Al$_2$O$_3$ shifted to a higher value (c.a. 5.4 Å^{-1}) compared to that in PdO, while the k value of Pt−O2 and Rh−O2 shifted to lower values (c.a. 3.5 and 3.6 Å^{-1}). The results suggest that the interaction of sub-adjacent oxygen atoms in Pd-nanoparticles and Pd in Pd/Al$_2$O$_3$ become stronger than that in PdO, these oxygen atoms could be more difficult to dissociate from the surface. However, surface oxygens in Pt/Al$_2$O$_3$ and Rh/Al$_2$O$_3$ were more accessible to remove. Since the location sites of PGM−O−Al are directly influenced by interfacial atoms in support, its distribution can be used for qualitatively comparing the intensity of MSI. As shown in Fig. 3g-i, the effect extent of Al to PGMs was as follows: Rh−O−Al > Pd−O−Al > Pt−O−Al, which is inversely with the order of cations distance of Al to PGMs. It indicates that the MSI in Rh/Al$_2$O$_3$ is stronger than that in Pd/Al$_2$O$_3$ and Pt/Al$_2$O$_3$, which is coincided with results of ^{1}H and ^{27}Al NMR spectra. In summary, PGM species loaded on γ-Al$_2$O$_3$ are the primary oxide state, but minor Pt and Pd in Pt/Al$_2$O$_3$ and Pd/Al$_2$O$_3$ are metallic due to an "excessive" grain size, respectively. It is also found that the intensity of MSI between PGMs and γ-Al$_2$O$_3$ in Rh/Al$_2$O$_3$ is also higher than that in Pd/Al$_2$O$_3$ and Pt/Al$_2$O$_3$.

3.4. NO reduction

NO reduction by CO under wet conditions is generally assumed to be one of the most typical model reactions of TWC. In the NO reduction process, both CO or H$_2$ can serve as reductants, these tests in the wet condition were firstly performed in this work[13]. As shown in Fig. 4a, Rh/Al$_2$O$_3$ generated more NH$_3$ than Pd/Al$_2$O$_3$ and Pt/Al$_2$O$_3$ at lower temperature (<300 °C), while Pt/Al$_2$O$_3$ provided more NH$_3$ than Pd/Al$_2$O$_3$ above 300 °C. This result should be attributed to reducibility of different PGMs (Fig. S3 and Tab. S5). One should note that all catalysts display a similar tendency in which NH$_3$ concentrations decreased to some extent. This can be resulted from occurring NH$_3$ decomposition under the oxygen-free condition. The NH$_3$ decomposition tests have
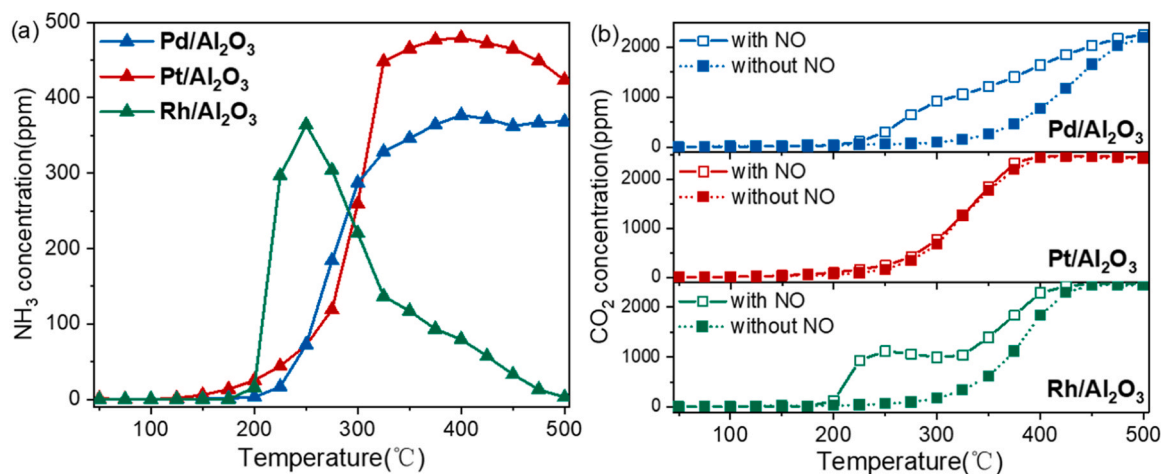

Fig. 4. The NH$_3$ formations under the simulated TWC flue gas (a); the influence of NO on the CO$_2$ formation (b). [CO] = 2500 ppm, [NO] = 500 ppm, [H$_2$O] = 2%, balanced by N$_2$ (triangle: NH$_3$; quadrate: CO$_2$).
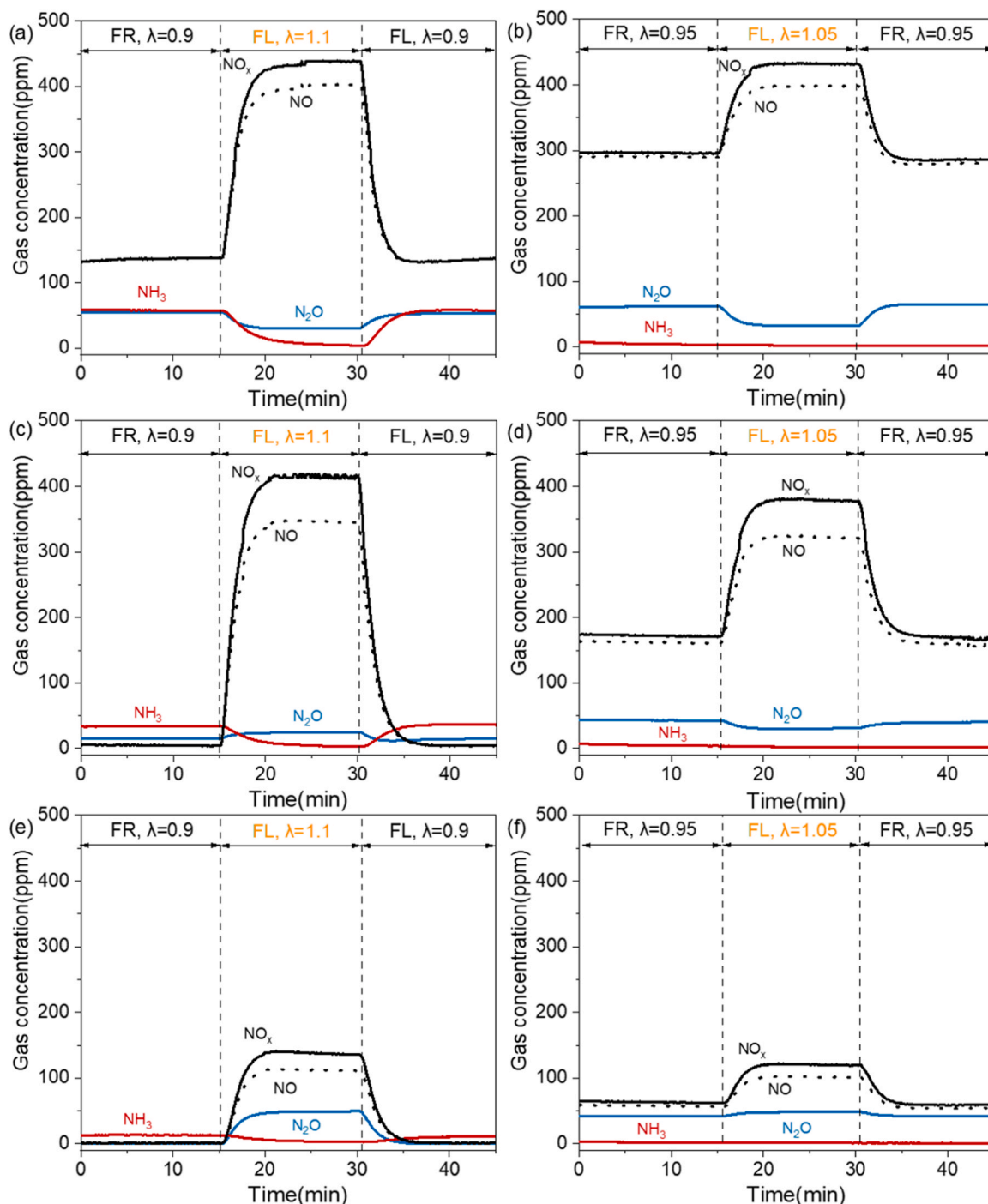
Fig. 5. The N_2O and NH_3 formations on Pd/Al_2O_3 (a, b), Pt/Al_2O_3 (c, d), and Rh/Al_2O_3 (e, f) under wide ($\lambda = 0.9/1.1$) and narrow ($\lambda = 0.95/1.05$) air-to-fuel working conditions at 350 °C. Gas concentration: [CO] = 10000 ppm, [NO] = 500 ppm, [C_3H_6] = 2000 ppm, [H_2O] = 2%, [O_2] = 13750 ppm ($\lambda = 1$), balanced by N_2 ($\lambda = 0.9$, [O_2] = 12300 ppm; λ=1.1, [O_2] = 14400 ppm; $\lambda = 0.95$, [O_2] = 13000 ppm; $\lambda = 1.05$, [O_2] = 12300 ppm. (FR: Fuel-Rich, FL: Fuel-Lean).

been carried out (Fig. S4). The Rh/Al_2O_3 catalyst exhibits an extraordinary capacity for NH_3 decomposition, resulting in no NH_3 formation above 300 °C. At lower temperature, Rh/Al_2O_3 was more likely to generate NH_3 but then they were more likely to decompose above 250 °C. These results suggest that Pt species could be more suitable than Pd species in minimizing NH_3 formations. Fig. 4b showed the influence of WGS reaction in wet conditions. The WGS reactions with NO of Pd/Al_2O_3 and Rh/Al_2O_3 were promoted compared to those without NO in 200–500 °C, indicating that the NO reduction promotes the WGS reaction in Pd/Al_2O_3 and Rh/Al_2O_3.

Since the air-fuel ratio (λ), calculated by the formula (6) in **SI**, has a

great influence on the byproduct formations in NO reduction, the corresponding experiments with λ-modulation were carried out (Fig. 5). Note that the dwell time at each condition was expanded (15 min) for better observing its influence on N_2O and NH_3 formation. When the atmospheres transfer from fuel-rich (FR) to fuel-lean (FL) conditions, NH_3 concentrations decreased but N_2O showed opposite tendencies on both Pt/Al_2O_3 and Rh/Al_2O_3. It may be caused by consumption of CO and undersupply of H_2. Under FL conditions, the WGS and hydrocarbon reforming reactions were suppressed, leading to a decrease in H_2 production. Since CO was more likely to be oxidized than WGS, NH_3 formation would be rapidly inhibited. Whereas the increase in N_2O could
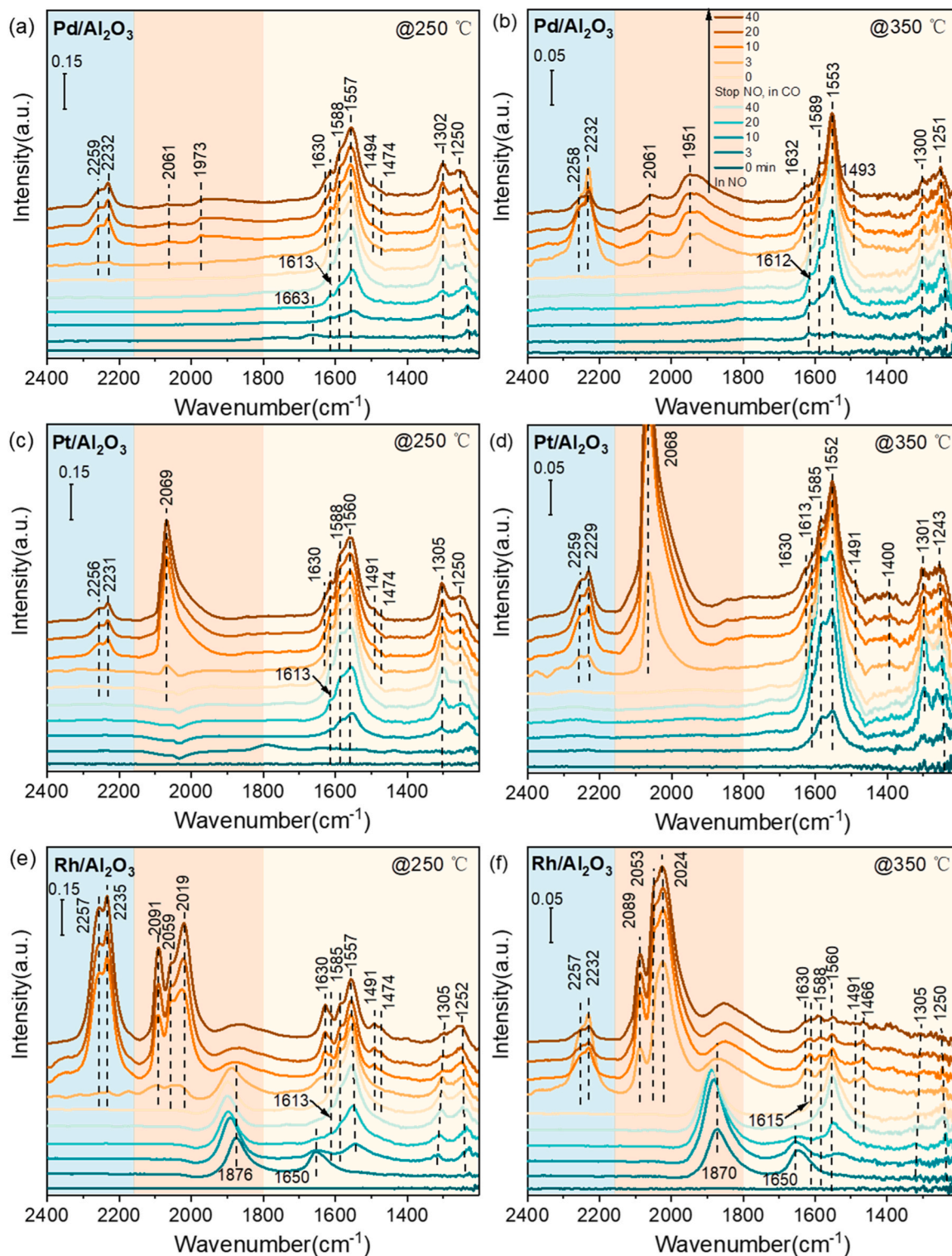
Fig. 6. In-situ DRIFTS spectra of Pd/Al$_2$O$_3$ (a, b), Pt/Al$_2$O$_3$ (c, d), and Rh/Al$_2$O$_3$ (e, f) pretreated by 500 ppm NO, N$_2$ purged, and then followed by exposing to 2500 ppm CO at 250 and 350 °C, respectively.

result from the direct NO reduction, but the hydrogenation of N$_2$O to NH$_3$ could be difficult due to the absence of H$_2$. Pd/Al$_2$O$_3$ showed slightly higher N$_2$O and NH$_3$ than Pt/Al$_2$O$_3$ with wider or narrower λ, and a higher NO$_x$ under FL conditions, especially with narrower λ. These results indicate that Pt/Al$_2$O$_3$ exhibits both better NO$_x$ removal efficiency and suppression of byproduct formation than Pd/Al$_2$O$_3$. Moreover, compared with the wider λ (0.9/1.1), the concentration of N$_2$O

with the narrower λ (0.95–1.05) is 50 ppm in the FR and FL conditions for Rh/Al$_2$O$_3$. Whereas, there is almost no NH$_3$ formation at different λ.

Considering the cost and superior NO reduction performance of Rh species, it is still necessary to add a small amount of Rh species to TWC recipes. Thereby, the two catalysts, PtRh/Al$_2$O$_3$ and PdRh/Al$_2$O$_3$, in which the molar ratios of Pt or Pd to Rh was 9:1, were synthesized and tested under simulated TWC conditions (λ=0.95) (Fig. S5). Both PtRh/
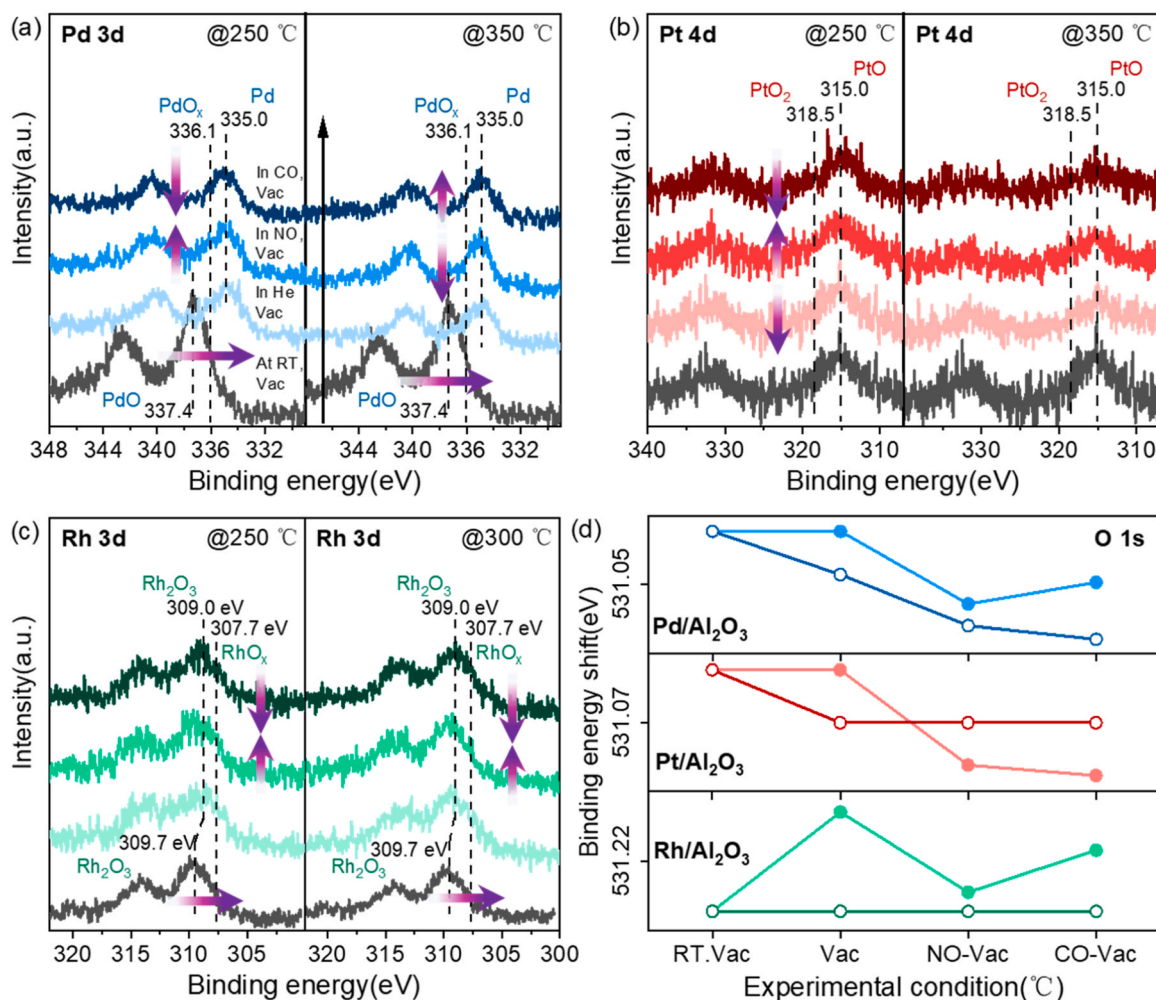
Fig. 7. In-situ NAP-XPS spectra of Pd 3d (a) at Pd/Al$_2$O$_3$, Pt 4d (b) at Pt/Al$_2$O$_3$, Rh 3d (c) at Rh/Al$_2$O$_3$, and (d) binding energy shift of O 1s from all samples in room temperature (RT) and then vacuumized, in He and vacuum, and then, 1 mbar NO and then vacuumized, and finally, 1 mbar CO and then vacuumized. (Solid circles: from RT to 250 °C. Hollow circles: from RT to 350 °C for Pd/Al$_2$O$_3$ & Pt/Al$_2$O$_3$; from RT to 300 °C for Rh/Al$_2$O$_3$).

Al$_2$O$_3$ and PdRh/Al$_2$O$_3$ showed similar CO and C$_3$H$_6$ oxidation activity but the PtRh/Al$_2$O$_3$ exhibited higher NO reduction activity and lower N$_2$O and NH$_3$ formations in steady-state test.

3.5. In-situ DRIFTS

The in-situ DRIFTS and NAP-XPS are performed to investigate NO reduction under dry conditions. According to N$_2$O and NH$_3$ formation behaviors, all measurements are performed at 250 and 350 °C. The adsorption species were listed in Tab. S6. At 250 °C, as soon as NO was introduced into the flue gas, monodentate, bidentate, and bridging nitrates as well as nitro and chelating nitro compounds can be observed (Fig. 6). Noteworthy that the intensities of nitro compounds in Pd/Al$_2$O$_3$ and Pt/Al$_2$O$_3$ are stronger than those in Rh/Al$_2$O$_3$. For Pd/Al$_2$O$_3$, trace Pd–N=O species with bent configuration appeared in 3 min, whereafter that disappeared in 10 min. This suggests that the Pd–N=O species are unstable on Pd/Al$_2$O$_3$. The Rh–N=O species in Rh/Al$_2$O$_3$ disappeared in 20 min (Fig. 6e), indicating that NO is likely to adsorb at the Rh and the adsorption species are more stable. The peaks in 1876–1900 cm^{-1} range can be assigned to dinitrosyl species (Rh(NO)$_2$–) corresponding to the symmetric vibration of cis-(NO)$_2$, and the blueshift occurred with increasing the adsorption time, which could result from the interaction with surface hydroxyls.

After CO was introduced into the flue gas, the intensities of nitrates, nitro, and chelating nitro compounds decreased slightly in Pd/Al$_2$O$_3$ and

Pt/Al$_2$O$_3$, indicating that these species can be partially reduced by CO. The appearance of new pair-peaks corresponding to N$_2$O suggests that N$_2$O forms on the surface of Pd/Al$_2$O$_3$ and Pt/Al$_2$O$_3$. However, the intensity of N$_2$O in Pt/Al$_2$O$_3$ is considerably lower than that in Pd/Al$_2$O$_3$. Combined with the results of N$_2$O formations at low temperature, Pt/Al$_2$O$_3$ does not yield N$_2$O under both dry (Fig. S6a) and wet conditions (Fig. 4a) below 300 °C. As for Rh/Al$_2$O$_3$, the peak of dinitrosyl species disappeared in 10 min and then became wide and flat, indicating that these species can be also reduced by CO to form adsorbed N$_2$O. Interestingly, the generated N$_2$O in Rh/Al$_2$O$_3$ is similar to that in Pd/Al$_2$O$_3$ in Fig. S6a. The results indicate that the decomposition of dinitrosyl species is mainly N$_2$ instead of N$_2$O and the adsorbed N$_2$O can be further reduced to N$_2$ because of the good reducibility of Rh species in Fig. S6 and S3a & b. In addition, Pt/Al$_2$O$_3$ presented another strong peak due to linear CO adsorbed on Pt (Pt–CO, 2069 cm^{-1}), while Rh/Al$_2$O$_3$ presented strong peaks due to gem-dicarbonyl species (–Rh(CO)$_2$, symmetric stretches: 2019 cm^{-1} and antisymmetric stretches: 2091 cm^{-1}) as well as a peak attributed to linear adsorbed CO (Rh–CO, 2059 cm^{-1}). As for Pd/Al$_2$O$_3$, only two weak peaks corresponding to linear CO adsorbed on Pd^0 (Pd^0–CO, 2061 cm^{-1}) and Pd$_2$–CO in a compressed (1973 cm^{-1}) were observed. These results indicate that Pt or Rh species have a good adsorbed ability for CO and show oxide states, but Pd species display bad ability and metallic state, which should originate from ultra-low dispersion of Pd species on γ-Al$_2$O$_3$. This strong adsorption to CO can facilitate the WGS reaction and thus promote NO

reduction, or N_2O reduction to N_2 in Fig. S6. Moreover, the NH_3 adsorption on the Lewis acid site ($\sim$1630 cm^{-1}, NH_3-L) and $-NH_2$ (1490–1495 cm^{-1}) were detected because of the reaction of N_2O with surface hydroxyls or even H_2. The intensity of NH_3-L in Rh/Al$_2$O$_3$ was significantly higher than that in Pd/Al$_2$O$_3$ and Pt/Al$_2$O$_3$. The shoulder peak (1474 cm^{-1}) can be due to the reduction of monodentate nitrate to its nitrite. Different from Pt/Al$_2$O$_3$ and Pd/Al$_2$O$_3$, the nitro compounds on Rh/Al$_2$O$_3$ occurred significantly decreasing.

At 350 °C, the bridging, bidentate, and monodentate nitrates on Pd/Al$_2$O$_3$ and Pt/Al$_2$O$_3$ occurred as soon as NO was introduced, and with increasing time, the monodentate nitrates became strong but bidentate nitrates became weak. This result indicates that monodentate nitrates are more stable than bridging or bidentate nitrates. The intensity of chelating nitro compounds on Pd/Al$_2$O$_3$ was stronger than that of nitro compounds. Moreover, only weak peaks of chelating nitro compounds were observed on Pt/Al$_2$O$_3$. The results indicate that, unlike the results at 250 °C, the two species on both Pd/Al$_2$O$_3$ and Pt/Al$_2$O$_3$ display distinct reactivity at 350 °C. As for Rh/Al$_2$O$_3$, the adsorption behaviors of nitrates, nitro compounds, chelating nitro compounds, Rh–N=O and dinitrosyl species showed similar features to those at 250 °C.

When CO was introduced into the flue gas, the weak peak of bridging nitrates almost disappeared and the peak intensity of monodentate nitrates and chelating nitro compound severely decreased, whereas the intensities of bidentate nitrates and nitro compounds increased. The results indicate that, among the adsorption species of NO, the chelating nitro compounds, bridging, and monodentate nitrates are the reactive intermediate species, whereas the nitro compounds and bidentate nitrate may suppress NO reduction. Compared with the results at 250 °C, the new peaks correlated to NH_3 species also appeared, indicating that some NH_3 species can form on Pd/Al$_2$O$_3$ and Pt/Al$_2$O$_3$ via reacting with surface hydroxyls. That is, Pt–CO or Pd–CO species exhibit excellent adsorption ability. As for Rh/Al$_2$O$_3$, the bridging and monodentate nitrates showed considerable decrease in 3 min, whereas the nitro compounds almost disappeared. The peak intensity of N_2O was stable after CO introduction in 10 min. The results indicate that nitrates, nitro compounds, and dinitrosyl species present higher activity than chelating nitro compounds at 350 °C.

In a word, the Rh/Al$_2$O$_3$ shows higher N_2O and NH_3 formations than those for Pt/Al$_2$O$_3$ and Pd/Al$_2$O$_3$, which is attributed to higher active intermediates, especially nitro compound and dinitrosyl species. Meanwhile, a discrepancy in N_2O generation performance for Pt/Al$_2$O$_3$ and Pd/Al$_2$O$_3$ (Fig. S6a) is closely related to their N_2O desorption capacity because both samples show similar changes in NO adsorption species especially at low temperature. Whereas, the vibration intensity of N_2O displays a big difference, namely, that on Pd/Al$_2$O$_3$ is rapidly increasing and then decreasing.

3.6. In-situ NAP-XPS

Fig. 7 shows the transformation of the chemical state corresponding to PGMs and lattice oxygen during the reaction process. The binding energy of all elements was calibrated at Al 2p (74.5 eV) in Fig. S7a-**c**. To observe changes in O 1s spectra, the related data were converted to the graphic of experimental condition–binding energy (Fig. 7**d**) and the originated profiles were presented in Fig. S7d-**f**. Different from detection at room temperature, PGMs were reduced to low valence states with increasing the temperatures. Pd species transferred from PdO (337.4 eV) to PdO$_x$ (Pd$^{\delta+}$, $0<\delta<2$, 336.1 eV) and metal state of Pd (Pd^0, 335.0 eV) in Pd/Al$_2$O$_3$ (Fig. 7a); the peak of PtO$_2$ (318.5 eV) became weak in Pt/Al$_2$O$_3$ (Fig. 7b); the peak of Rh species downshifted from 309.7 to 309.0 eV and the RhO$_x$ (Rh$^{\beta+}$, 307.7 eV) appeared in Rh/Al$_2$O$_3$ (Fig. 7c). These results can be attributed to the thermal decomposition of metal oxides (Fig. S3b). Noteworthy that the variation extent of Pd and Rh species are much bigger than that of Pt species, proving that their oxides possess superior reducibility and self-decomposition ability under the free-oxygen environment.

When NO was introduced at 250 °C, the peak intensity of PdO$_x$ became stronger (Pd$^0\rightarrow$Pd$^{\delta+}$) and the binding energy of O 1s downshifted in Pd/Al$_2$O$_3$ (Fig. 7a & d), suggesting the electron transfer from NO and Pd to O$_L$. As soon as NO was removed and CO was introduced, the peak intensity of PdO$_x$ decreased (Pd$^{\delta+}\rightarrow$Pd^0) and the peak of O 1s upshifted but still located at lower binding energy, indicating that both Pd species (Pd$^{\delta+}$/Pd^0) and O$_L$ participate in NO reduction. At 350 °C, the peak intensity of PdO$_x$ decreased (Pd$^{\delta+}\rightarrow$Pd^0) with a downshift of O 1s when NO introduction and then it recovered (Pd$^0\rightarrow$Pd$^{\delta+}$) with a further downshift of O 1s after CO introduction. The results indicate that Pd species (Pd$^{\delta+}$/Pd^0) and oxygen atoms also play roles of electron reservoir during the NO reduction process at high temperature, suggesting that a rapid reaction process is occurring and further promoting the reduction of NO adsorption species to a low valence state, like N_2O and N_2, etc.

Concerning Pt/Al$_2$O$_3$ in Fig. 7b & d, when NO was introduced at 250 °C, the peak intensity of PtO$_2$ became stronger (Pt$^{2+}\rightarrow$Pt^{4+}) with downshift of O 1s peak, indicating that the electron transfer from NO and Pt species to O$_L$. With the introduction of CO, the electrons were back to Pt species, leading to an increase of PtO peak intensity (Pt$^{4+}\rightarrow$Pt^{2+}). The products were mainly N_2 instead of N_2O due to the excessively adsorbed on Pt/Al$_2$O$_3$ (Fig. 6c and Fig. S6). The changes of Pt species at 350 °C showed similar changes but the binding energy of O 1s was almost unchanged. This result indicates that O$_L$ is not participated in the reaction.

As for Rh/Al$_2$O$_3$ (Fig. 7c & d), when NO was introduced at 250 °C, the peak intensity of RhO$_x$ (Rh$^{3+}\rightarrow$Rh$^{\beta+}$) became stronger along with O 1s downshifts, suggesting that these electrons can transfer to Rh species and O$_L$ caused by adsorbing NO. After CO introduction, NO adsorption species with higher valence state converted to nitrites, NH_3 species, or N_2O, the peak of RhO$_x$ decreased (Rh$^{\beta+}\rightarrow$Rh^{3+}) and the peak of O 1s upshifted in Fig. 7c & d. These results indicate that both Rh species and O$_L$ are involved in the NO reduction. When the temperature was higher than 300 °C, Rh species showed similar changes compared with those at 250 °C in Fig. 7**c**, but there was almost no change to occur in the O 1s peak (Fig. 7d) after NO and CO introduction. This result indicates that Rh species can act as electron reservoirs due to NO oxidation (NO $\rightarrow$ nitrates or nitrites) and further in NO reduction reaction, whereas the O$_L$ in Rh Rh/Al$_2$O$_3$ does not serve as active species above 300 °C.

Pd, Pt, and Rh on γ-Al$_2$O$_3$ can be involved in the adsorption and reduction process of NO via a pair of metal cations (Pt$^{2+}\leftrightarrow$Pt^{4+}in Pt/Al$_2$O$_3$, Pd$^{\delta+}\leftrightarrow$Pd^0 in Pd/Al$_2O_3$, Rh$^{\beta+}\leftrightarrow$Rh^{3+} in Rh/Al$_2O_3$). Pd and Rh species function as relay stations for electron transfer during NO adsorption and reduction, especially at high temperature. The O$_L$ plays the same role at the low temperature (250 °C). However, as the temperature increases, the O$_{latt}$ becomes relatively inert and cease active participation in the reaction. This inertness of O$_L$ hinders oxygen mobility or dissociation, making N_2O difficult to desorb from the surface of samples.

3.7. Influence of H_2O

It has been reported that the introduction of H_2O can provide extra reductant (hydrogen) by WGS for NO reduction, which results in NH_3 and N_2O formations.[13] The in-situ DRIFTS spectra of the catalysts are shown in Fig. S8. When H_2O was introduced into the flue gas, the peaks corresponding to N_2O and bridging nitrates for both Pd/Al$_2$O$_3$ and Pt/Al$_2$O$_3$ quickly disappeared. Meanwhile, the peak of NH_3–L weakened, accompanied by the appearance of –NH species. This suggests that surface NH_3–L and –NH species could be crucial rate-determining intermediates in NO reduction under wet condition. As for Rh/Al$_2$O$_3$, the variations in N_2O and NH_3 were similar to those observed in Pt/Al$_2$O$_3$. However, the bridging and bidentate nitrates still observed, while the monodentate nitrates almost disappeared. These results indicate that the monodentate nitrates are highly active in NH_3 generation. Moreover, the Rh(CO)$_2$– species completely disappeared, and thus the Rh–CO species
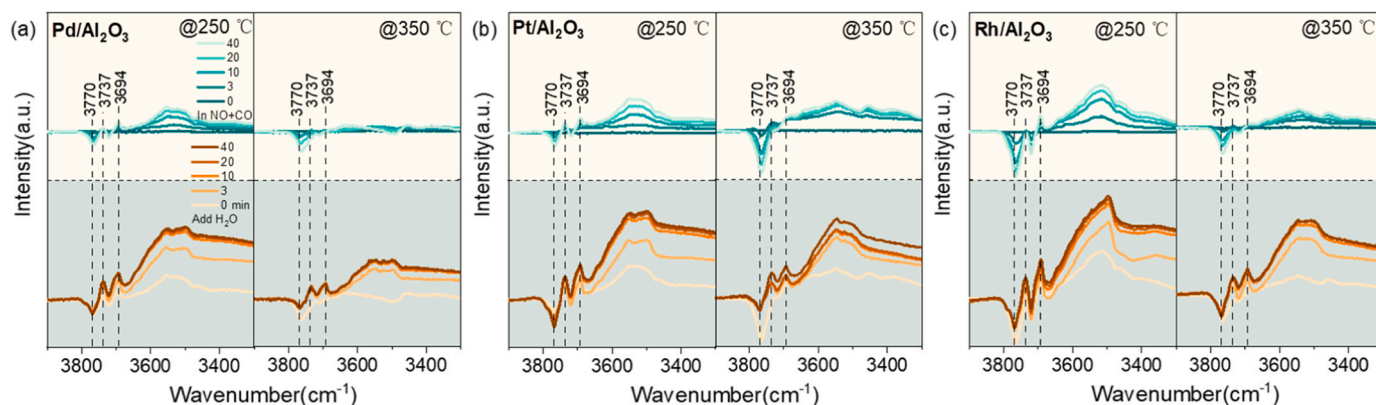
Fig. 8. In-situ DRIFTS spectra of hydroxyl and amino groups on Pd/Al$_2$O$_3$ (a), Pt/Al$_2$O$_3$ (b), and Rh/Al$_2$O$_3$ (c) during NO+CO reaction with H$_2$O at 250 and 350 °C, respectively.

became distinct, suggesting that the former are highly active intermediate species in the WGS reaction.

The hydroxyl and amino formation regions from in-situ DRIFTS spectra are shown in Fig. 8. The negative peak at 3770 cm^{-1} could be attributed to the terminal hydroxyls (HO$_I$), and the positive peaks at 3737 and 3694 cm^{-1} could be attributed to the doubly-bridged (HO$_{II}$) and triply-bridged (HO$_{III}$) hydroxyls, respectively. When NO and CO were introduced into the flue gas, the peak of HO$_I$ decreased but the peaks of HO$_{II}$ and HO$_{III}$ slightly increased, suggesting that HO$_I$ participates in reaction with CO, among a small amount which convert HO$_{II}$ and HO$_{III}$. Noteworthy that the peak intensity of HO$_I$ in Rh/Al$_2$O$_3$ was much lower than that in Pd/Al$_2$O$_3$ and Pt/Al$_2$O$_3$ at the low temperature, leading to more NH$_3$ species formation (Fig. S8). In contrary, the peak intensity of HO$_I$ in Pt/Al$_2$O$_3$ becomes lowest above 350 °C. The increase of HO$_I$ activity also promoted the formation of NH$_3$ species. All catalysts showed a lightly recovery for the peak intensities of HO$_I$ and HO$_{II}$ by H$_2$O introduction, while only the HO$_I$ in Rh/Al$_2$O$_3$ showed a distinct re-heal at the low temperature. This suggests relatively high regeneration ability, leading to more NH$_3$ species formation (Fig. S8) and NH$_3$ yield (Fig. 4a). Obviously, all hydroxyl group show regeneration with temperature increasing, which results in more NH$_3$ formation. However, the HO$_I$ consumption extent on Rh/Al$_2$O$_3$ at high temperature becomes lower than that at low temperature, suggesting that NH$_3$ formation could become more difficult.

In a word, both adsorbed NO$_x$ species and N$_2$O on the surface are active intermediate species for NH$_3$ formation. Highly-active bridging nitrates and terminal hydroxyls are the main reasons of highest NH$_3$ formation activity on Rh/Al$_2$O$_3$ at low temperature. Furthermore, NH$_3$ formation is closely related to the activity of surface hydroxyls for all catalysts. The highly-active hydroxyls as well as their regeneration ability, especially HO$_I$, are crucial active species during the NH$_3$ formation.

4. Conclusions

The Pd/, Pt/, and Rh/Al$_2$O$_3$ (~1.0 wt%) catalysts have been prepared to investigate the effect of PGMs on NH$_3$ formation in NO reduction by CO. XAFS and NMR spectra of ^{1}H and ^{27}Al prove that the anchoring of Pd, Pt, and Rh on γ-Al$_2$O$_3$ will slightly changes coordination environment of tetrahedral (Al$_{tetra}^{3+}$) and pentahedral (Al$_{penta}^{3+}$) Al via consuming triply bridging hydroxyls and newly forming doubly bridging hydroxyls (PGMs–(HO)–Al$_n$), leading to the intensity of PGMs/Al$_2$O$_3$ as follows: Rh/Al$_2$O$_3$ > Pd/Al$_2$O$_3$ > Pt/Al$_2$O$_3$. Thus, Rh/Al$_2$O$_3$ displays the most exceptional reducibility and oxygen desorption capacity, whereas Pd/Al$_2$O$_3$ exhibits better oxygen desorption capacity and worse reducibility than Pt/Al$_2$O$_3$ due to stronger oxygen activation. Rh/Al$_2$O$_3$ shows more NH$_3$ formation at low temperature, which is attributed to the

higher reactivity of intermediates. Whereas at high temperature the significant NH$_3$ decrease can be due to their superior NH$_3$ decomposition performance.

Hence, the Pt$_{0.9}$Rh$_{0.1}$/Al$_2$O$_3$ catalyst presented both higher TWC performance and byproduct suppression than Pd$_{0.9}$Rh$_{0.1}$/Al$_2$O$_3$ under simulated TWC condition. This study elucidates the interaction mechanism of the different PGMs and γ-Al$_2$O$_3$. It also reveals the intricate relationship between byproduct formation and these features, providing an effective strategy for optimizing TWC recipes of gasoline catalysts.

CRediT authorship contribution statement

Wenzhe Si: Data curation. **Jin Yuan:** Supervision, Investigation, Conceptualization. **Chuan Gao:** Supervision, Investigation, Conceptualization. **Rong Wang:** Supervision, Investigation, Conceptualization. **Bin Zhou:** Data curation. **Junhua Li:** Writing – review & editing, Writing – original draft, Project administration, Investigation, Funding acquisition, Conceptualization. **Yunlong Wang:** Conceptualization, Investigation, Supervision. **Houlin Wang:** Writing – review & editing, Writing – original draft, Investigation, Conceptualization. **Yue Peng:** Writing – review & editing, Writing – original draft, Project administration, Investigation, Funding acquisition, Conceptualization.

Declaration of Competing Interest

The authors declare that they have no known competing financial interests or personal relationships that could have appeared to influence the work reported in this paper.

Data availability

No data was used for the research described in the article.

Appendix A. Supporting information

Supplementary data associated with this article can be found in the online version at doi:10.1016/j.apcatb.2024.124009.

References

[1] A. Wang, L. Olsson, The impact of automotive catalysis on the united nations sustainable development goals, Nat. Catal. 2 (2019) 566–570.

[2] N.W. Cant, D.E. Angove, D.C. Chambers, Nitrous oxide formation during the reaction of simulated exhaust streams over rhodium, platinum and palladium catalysts, Appl. Catal. B-Environ. 17 (1998) 63–73.

[3] C. Wang, J. Tan, G. Harle, H. Gong, W. Xia, T. Zheng, D. Yang, Y. Ge, Y. Zhao, Ammonia formation over Pd/Rh three-way catalysts during lean-to-rich fluctuations: the effect of the catalyst aging, exhaust temperature, lambda, and duration in rich conditions, Environ. Sci. Technol. 53 (2019) 12621–12628.

[4] G.Q. Chen, B. Zhang, Greenhouse gas emissions in China 2007: inventory and input-output analysis, Energ. Policy 38 (2010) 6180–6193.

[5] Y.-C. Lin, M.-T. Cheng, W.-Y. Ting, C.-R. Yeh, Characteristics of gaseous HNO_2, HNO_3, NH_3 and particulate ammonium nitrate in an urban city of Central Taiwan, Atmos. Environ. 40 (2006) 4725–4733.

[6] Z. Zhang, Y. Yan, S. Kong, Q. Deng, S. Qin, L. Yao, T. Zhao, S. Qi, Benefits of refined NH_3 emission controls on $PM_{2.5}$ mitigation in central China, Sci. Total Environ. 814 (2022) 151957.

[7] Z. Lei, J. Zhang, M. Zhou, C. Braun, M. Schmidt, J.M. Richter, S. Batke, Secondary emission control towards post China 6 legislation, SAE Technical Paper, 2021.

[8] N.J. Farren, J. Davison, R.A. Rose, R.L. Wagner, D.C. Carslaw, Underestimated ammonia emissions from road vehicles, Environ. Sci. Technol. 54 (2020) 15689–15697.

[9] C.D. DiGiulio, J.A. Pihl, J.E. Parks II, M.D. Amiridis, T.J. Toops, Passive-ammonia selective catalytic reduction (SCR): understanding NH_3 formation over close-coupled three way catalysts (TWC), Catal. Today 231 (2014) 33–45.

[10] J.R. Theis, J. Kim, G. Cavataio, Passive TWC+SCR systems for satisfying Tier 2, Bin 2 emission standards on lean-burn gasoline engines, SAE Int. J. Fuels Lubr. 8 (2015) 460–473.

[11] S. Yasumura, T. Kato, Y. Qian, T. Toyao, Z. Maeno, K.-i Shimizu, Dynamic structural evolution of $[Rh(NO)_2]^+$ complex/Rh metal cluster in zeolite during de-NO_x via *in Situ* formed NH_3 under lean/rich periodic conditions, J. Phys. Chem. C. 126 (2022) 19147–19158.

[12] E.C. Adams, M. Skoglundh, M. Folic, E.C. Bendixen, P. Gabrielsson, P.-A. Carlsson, Ammonia formation over supported platinum and palladium catalysts, Appl. Catal. B-Environ. 165 (2015) 10–19.

[13] H. Wang, Y. Peng, B. Zhou, J. Yuan, R. Wang, W. Si, J. Li, Formation mechanisms of N_2O and NH_3 on Pd/ZrO_2 and Pd/Al_2O_3 for NO reduction, Chem. Eng. J. (2023) 145379.

[14] C. Wang, W. Xia, Y. Zhao, New insight into hydroxyl-mediated NH_3 formation on the Rh-CeO_2 catalyst surface during catalytic reduction of NO by CO, Chin. J. Catal. 38 (2017) 1399–1405.

[15] Y. Qian, X. Wei, Y. Sun, F. Tang, S. Meng, L. Qiu, T. Wang, B. Ye, T. Pan, Y. Zhang, Investigation of the formation characteristics of N_2O and NH_3 for stoichiometric natural gas engines with Pd-only catalyst, Fuel 329 (2022) 125223.

[16] S. Yasumura, K. Nagai, Y. Qian, T. Toyao, Z. Maeno, K.-i Shimizu, Multi-functionality of rhodium-loaded MOR zeolite: Production of H_2 *via* the water gas shift reaction and its use in the formation of NH_3, Catal. Sci. Technol. 13 (2023) 2994–3000.

[17] R.J. Farrauto, M. Deeba, S. Alerasool, Gasoline automobile catalysis and its historical journey to cleaner air, Nat. Catal. 2 (2019) 603–613.

[18] H. Li, Y. Shen, X. Xiao, H. Jiang, Q. Gu, Y. Zhang, L. Lin, W. Luo, S. Zhou, J. Zhao, A. Wang, T. Zhang, B. Yang, Controlled-release mechanism regulates rhodium migration and size redistribution boosting catalytic methane conversion, ACS Catal. 13 (2023) 1197–1206.

[19] Y. Ren, D. Lou, P. Tan, Y. Zhang, X. Sun, Emission reduction characteristics of after-treatment system on natural gas engine: effects of platinum group metal loadings and ratios, J. Clean. Pro. 298 (2021) 126833.

[20] C. Wang, W. Xia, D. Yang, T. Zheng, Y. Rong, J. Du, B. Wu, Y. Zhao, Paper understanding ammonia and nitrous oxide formation in typical three-way catalysis during the catalyst warm-up period, J. Hazard. Mater. 438 (2022) 129553.

[21] J.H. Kwak, J. Hu, D. Mei, C.-W. Yi, D.H. Kim, C.H.F. Peden, L.F. Allard, J. Szanyi, Coordinatively unsaturated Al^{3+} centers as binding sites for active catalyst phases of platinum on γ-Al_2O_3, Science 325 (2009) 1670–1673.

[22] K. Murata, Y. Mahara, J. Ohyama, Y. Yamamoto, S. Arai, A. Satsuma, The metal-support interaction concerning the particle size effect of Pd/Al_2O_3 on methane combustion, Angew. Chem. Int. Ed. 56 (2017) 15993–15997.

[23] J.H. Kwak, J.Z. Hu, D.H. Kim, J. Szanyi, C.H.F. Peden, Penta-coordinated Al^{3+} ions as preferential nucleation sites for BaO on γ-Al_2O_3: an ultra-high-magnetic field ^{27}Al MAS NMR study, J. Catal. 251 (2007) 189–194.

[24] H. Deng, Y. Yup, H. He, Water effect on preparation of Ag/Al_2O_3 catalyst for reduction of NO_x by ethanol, J. Phys. Chem. C. 120 (2016) 24294–24301.

[25] Y. Xiao, S. Xu, X. Wang, Z. Lu, C. Hu, J. Li, *Enteromorpha prolifera* valorization to acetol over supported Pd catalysts: role of the support, Chem. Eng. J. 475 (2023) 146295.

[26] F. Wang, J. Ma, S. Xin, Q. Wang, J. Xu, C. Zhang, H. He, X.C. Zeng, Resolving the puzzle of single-atom silver dispersion on nanosized γ-Al_2O_3 surface for high catalytic performance, Nat. Commun. 11 (2020) 529.

[27] Z. Zhao, D. Xiao, K. Chen, R. Wang, L. Liang, Z. Liu, I. Hung, Z. Gan, G. Hou, Nature of five-coordinated Al in γ-Al_2O_3 revealed by ultra-high-field solid-state NMR, ACS Cent. Sci. 8 (2022) 795–803.

[28] M. Taoufik, K.C. Szeto, N. Merle, I. Del Rosal, L. Maron, J. Trebosc, G. Tricot, R. M. Gauvin, L. Delevoye, Heteronuclear NMR spectroscopy as a surface-selective technique: a unique look at the hydroxyl groups of γ-alumina, Chem. -Eur. J. 20 (2014) 4038–4046.

[29] D.F. Khabibulin, E. Papulovskiy, A.S. Andreev, A.A. Shubin, A.M. Volodin, G. A. Zenkovets, D.A. Yatsenko, S.V. Tsybulya, O.B. Lapina, Surface hydroxyl OH defects of η-Al_2O_3 and χ-Al_2O_3 by solid state NMR, XRD, and DFT calculations, Z. Phys. Chem. 231 (2017) 809–825.

[30] C. Wang, F. Feng, J. Du, T. Zheng, Z. Pan, Y. Zhao, Activation of surface lattice oxygen in ceria supported Pt/Al_2O_3 catalyst for low-temperature propane oxidation, ChemCatChem 11 (2019) 2054–2057.

[31] G. Busca, E. Finocchio, V. Sanchez Escribano, Infrared studies of CO oxidation by oxygen and by water over Pt/Al_2O_3 and Pd/Al_2O_3 catalysts, Appl. Catal. B-Environ. 113 (2012) 172–179.

[32] Y. Shan, G. He, J. Du, Y. Sun, Z. Liu, Y. Fu, F. Liu, X. Shi, Y. Yu, H. He, Strikingly distinctive NH_3-SCR behavior over Cu-SSZ-13 in the presence of NO_2, Nat. Commun. 13 (2022) 4606.

[33] V.L. Sushkevich, O.V. Safonova, D. Palagin, M.A. Newton, J.A. van Bokhoven, Structure of copper sites in zeolites examined by fourier and wavelet transform analysis of EXAFS, Chem. Sci. 11 (2020) 5299–5312.

[34] H. Xu, Z. Zhang, J. Liu, D.-T. Chi-Linh, H. Chen, S. Xu, Q. Lin, Y. Jiao, J. Wang, Y. Wang, Y. Chen, S. Dai, Entropy-stabilized single-atom Pd catalysts via high-entropy fluorite oxide supports, Nat. Commun. 11 (2020) 3908.